Green Chemistry

ROYAL SOCIETY OF CHEMISTRY

COMMUNICATION

View Article Online
View Journal | View Issue

Cite this: *Green Chem.*, 2022, **24**, 1090

Received 1st December 2021,
Accepted 6th January 2022

DOI: 10.1039/d1gc04483d

rsc.li/greenchem

Boosting nitrate electroreduction to ammonia on NbO$_x$ *via* constructing oxygen vacancies†

Xuefei Wan,[a] Weiwei Guo,[b] Xue Dong,[a] Haihong Wu, *[a] Xiaofu Sun, *[b] Mengen Chu,[a] Shitao Han,[a] Jianxin Zhai,[a] Wei Xia,[a] Shuaiqiang Jia, [a] Mingyuan He[a] and Buxing Han *[a,b]

We have synthesized NbO$_x$ with oxygen vacancies (OVs) and conducted the first work on nitrate electroreduction to NH$_3$ over Nb oxides. It is a robust non-precious metal catalyst for NH$_3$ synthesis by nitrate electroreduction. The faradaic efficiency of 94.5% and the NH$_3$ formation rate of 55.0 μg h^{-1} mg$_{cat}$$^{-1}$ were achieved in a neutral electrolyte. The excellent performance of NbO$_x$ originates from the intrinsic properties of Nb oxides and the OVs in the catalyst.

Ammonia (NH$_3$) is a vitally important common chemical.[1–3] It has been widely used as a raw feedstock for producing fertilizers to sustain the population of the world.[4–7] On the other hand, NH$_3$ is widely used in the textile industry, plastics, and the pharmaceutical industry.[8] It is also increasingly recognized as a next-generation green energy carrier and an ideal carbon-free fuel.[9] Currently, NH$_3$ is synthesized by the conventional Haber–Bosch process using Fe-based catalysts at a high temperature (350–550 °C) and high pressure (150–300 atm).[4,8] Approximately 2% of the total global fossil energy is consumed in NH$_3$ production. In addition, the high-purity hydrogen used in the reaction is obtained from the steam reforming of fossil fuels, mainly natural gas, causing an enormous amount of CO$_2$ emission into the atmosphere.[10,11] It is imperative to develop alternative approaches that can overcome the limitations of the Haber–Bosch process including harsh conditions, high energy consumption, and negative environmental impacts.[4,10,12]

In recent decades, excessive nitrate has been found in the biosphere, and is discharged into the surface and underground water. The accumulation of nitrate can not only cause serious health problems, but also induce acid rain and photochemical smog.[13–15] This situation will further deteriorate due to the widespread use of nitrogen fertilizers in agriculture and massive sewage discharge from the industry. There is a strong need for developing an efficient approach to solve the problem of nitrate contamination. Recently, the electrocatalytic nitrate reduction reaction (NITRR) into NH$_3$ using water as the hydrogen source has attracted much attention due to its economic potential competition and ecofriendly advantages,[5,16–18] and is a wise strategy from the perspective of environmental protection and energy saving. However, the complicated eight-electron reduction course from nitrate to NH$_3$ and the competitive hydrogen evolution reaction (HER) inhibit its high selectivity and efficiency.[2,5,19] Therefore, designing efficient electrocatalysts with low cost and high activity and selectivity is extremely critical.

Nb-Based compounds are promising in heterogeneous catalysis.[20] NbO$_2$ is well regarded as a semiconductor with high capacitance and excellent electrical conductivity.[21] In addition, Nb$_2$O$_5$ was reported as a good promoter for beneficial ammonia synthesis under harsh conditions.[20] Thus, Nb oxides are expected to be promising NITRR electrocatalysts because the partially occupied d-orbitals of Nb^{4+} can form π backbonding with reactants.[21] Oxygen vacancies (OVs) in semiconducting materials have been widely used in the field of electro(photo)catalysis. Theoretical and experimental studies have reported that OVs in metal oxide catalysts could capture substrates, promote the electron transfer,[13] tailor the charge distribution[22] and enhance the chemisorption of molecules by offering coordinatively unsaturated sites.[23] Therefore, it is expected that OVs in metal oxides can availably capture and activate nitrate and thus possibly enhance the NITRR efficiency.

Herein, we report the first work to construct a NbO$_x$ catalyst with oxygen vacancies (OVs) for NITRR to NH$_3$. The catalyst exhibited a high faradaic efficiency (FE) of 94.5% and an NH$_3$ formation rate of 55.0 μg h^{-1} mg$_{cat}$$^{-1}$. A detailed study indi-

---

[a] Shanghai Key Laboratory of Green Chemistry and Chemical Processes, School of Chemistry and Molecular Engineering, East China Normal University, Shanghai 200062, China. E-mail: hhwu@chem.ecnu.edu.cn, hanbx@iccas.ac.cn

[b] Beijing National Laboratory for Molecular Sciences, CAS Key Laboratory of Colloid and Interface and Thermodynamics, CAS Research/Education Center for Excellence in Molecular Sciences, Institute of Chemistry, Chinese Academy of Sciences, Beijing 100190, China. E-mail: sunxiaofu@iccas.ac.cn

† Electronic supplementary information (ESI) available: Experimental procedures, Fig. S1–S10 and Table S1. See DOI: 10.1039/d1gc04483d

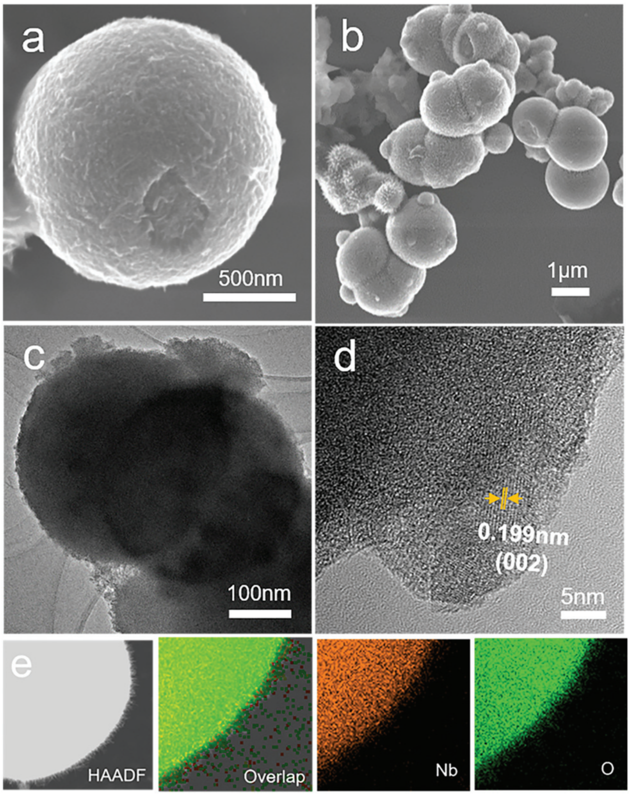

Fig. 1 (a and b) SEM images of NbO_x. (c and d) TEM and HRTEM images of NbO_x. (e) EDX elemental mapping images of Nb and O for NbO_x.

cated that the OVs affected the chemical state of Nb, which can improve the binding energy of key intermediates during the electrolysis.

The NbO_x catalyst was prepared through a simple hydrothermal method using niobium oxalates and oxalic acid as raw materials, and the detailed procedure is provided in the ESI.† No N element was included during the entire synthesis process of the catalysts. From the scanning electron microscopy (SEM) images in Fig. 1a and b, we can see that the synthesized NbO_x consists of well-distributed microspheres with an average diameter of 1.6 μm and they have a rough surface.[21,24] Fig. 1c shows the transmission electron microscopy (TEM) image of NbO_x, further indicating its sphere-like morphology.[20,24] The high-resolution TEM (HRTEM) image in Fig. 1d shows that the NbO specific lattice spacing of the (002) facet is 0.199 nm, which is in agreement with the reported data.[20,21] Elemental distribution mappings in Fig. 1e show the distributions of Nb and O, suggesting their homogenous distribution over the entire architectures. Nb_2O_5 particles were also prepared and the procedure is also provided in the ESI.† The SEM images of the synthesized Nb_2O_5 and commercial Nb_2O_5 (c-Nb_2O_5) particles are given in Fig. S1 and S2.†

The X-ray diffraction (XRD) patterns in Fig. 2a reveal that the diffraction peaks of the as-prepared NbO_x and Nb_2O_5 can be assigned to Nb_2O_5 (JCPDS no. 27-1003).[14] X-ray photoelectron spectroscopy (XPS) spectra further show the composition and chemical nature of the as-prepared materials. For NbO_x (Fig. 2b), the Nb 3d orbital can be resolved into two compositions, and each component consists of a spin–orbit pair with a separation energy of 2.7 eV. Both the Nb $3d_{3/2}$ and $3d_{5/2}$ peaks are found between the Nb^{IV} and Nb^{V} species, including the peaks belonging to Nb^{IV} (Nb $3d_{3/2}$ 209.7 eV; Nb $3d_{5/2}$ 206.5 +eV) and Nb^{V} (Nb $3d_{3/2}$ 210.6 eV; Nb $3d_{5/2}$ 207.8 eV). This showed the distinct change in the electronic structure compared to Nb_2O_5 (Fig. 2c).

To confirm the presence of OVs in NbO_x, Raman spectroscopy, XPS, photoluminescence (PL) spectroscopy and electron paramagnetic resonance (EPR) spectroscopy were further performed.[13] The Raman spectra of NbO_x and Nb_2O_5 are pre-

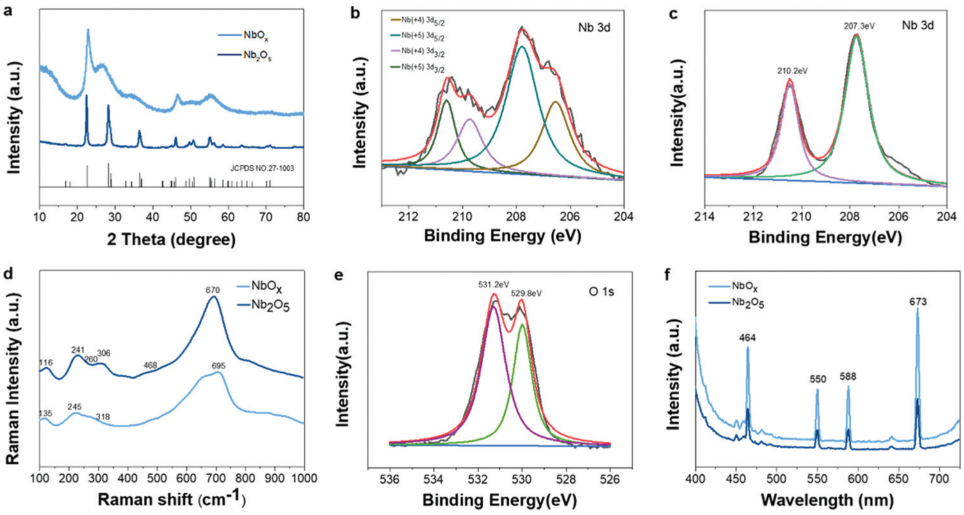

Fig. 2 (a) XRD patterns of NbO_x and Nb_2O_5. (b and c) XPS spectra of the Nb 3d orbital for NbO_x and Nb_2O_5. (d) Raman spectra of NbO_x and Nb_2O_5. (e) XPS spectra of the O 1s orbital for NbO_x. (f) PL spectra of NbO_x and Nb_2O_5.

sented in Fig. 2d. It can be seen that the peaks of NbO_x show a significant shift to the higher binding energy site compared to those of Nb_2O_5. These shifts can be ascribed to surface phonon confinement due to the existence of OVs in the NbO_x surface structure. All of these results clearly verified the NbO_x structure.[13,25–27] The peak at 529.8 eV in the O 1s orbit spectrum (Fig. 2e) can be assigned to lattice oxygen in NbO_x. Another peak at the binding energy of 531.2 eV can be attributed to the oxygen vacancies (OVs) on the NbO_x surface.[28] The XPS spectrum of O 1s for Nb_2O_5 is presented in Fig. S3.† The single peak at 530.5 eV is in accord with the O^{2-} in the Nb_2O_5 catalyst. The concentration of OVs was detected from the PL spectra with an excitation wavelength of 380 nm (Fig. 2f). It can be observed that NbO_x exhibits stronger photoluminescence at a wavelength of 588 nm, suggesting that it possesses a higher concentration of OVs compared with Nb_2O_5.[29–31] In the meantime, NbO_x exhibits a stronger EPR signal ($g = 2.00$) (Fig. S4, ESI†), indicating that rich OVs have been introduced into NbO_x.[13,32] All of these characterization results have justified the successful preparation of the NbO_x catalyst with OVs.

The electrocatalytic reduction of nitrate activity of NbO_x was carried out using an H-type cell with a standard three-electrode system at room temperature and atmospheric pressure. The catalysts loaded on carbon paper acted as the working electrode for the test. The electrochemical experiments were performed in Ar-saturated 0.5 M K_2SO_4 aqueous solution with 1000 ppm nitrate. The detailed experimental procedures are discussed in the ESI.† All potentials were with reference to the reversible hydrogen electrode (RHE). The concentration of reduction products was determined at the end of each electrolysis according to the indophenol blue method (ESI†). The standard calibration curves of NH_3 are shown in Fig. S5.†

The electrocatalytic performance was first evaluated by linear sweep voltammetry (LSV). Fig. 3a shows the LSV curves for NbO_x in Ar-saturated K_2SO_4 solutions with or without nitrate. The obvious increase of current density in the presence of nitrate could be observed, indicating that the nitrate in solution actually participated in the reduction reactions. These results confirm that NbO_x is an active electrocatalyst for electrochemical nitrate reduction.

To further analyze the reduction products, controlled potential electrolysis at each potential was performed to obtain the FE and the corresponding formation rate of NH_3 (Fig. 3b and c). The gas and liquid products were determined by gas chromatography and ultraviolet-visible (UV-vis) spectroscopy, respectively. The results showed that H_2 was the only by-product in the gas phase, and no other liquid by-products can be detected except for ammonia. From −0.55 V to −1.15 V *vs.* RHE, the NH_3 formation rates of three samples gradually increased, while the FE displayed volcanic-shape trends. The maximum FE of NH_3 over NbO_x was achieved at −0.75 V *vs.* RHE, which could reach 94.5% with the formation rate of 12 μg h^{-1} $mg_{cat}{}^{-1}$. Clearly, the NH_3 formation rate and FE increased when the negative potential increased up to −0.75 V. Beyond this negative potential, the FE decreased significantly because the hydrogen evolution reaction (HER) became the predominant process at the cathode. Electroreduction measurements were also conducted for Nb_2O_5 and c-Nb_2O_5 under the same conditions for comparison, and they showed lower catalytic performance than NbO_x (Fig. 3b and c). The highest FE of NH_3 was only 53.8% and 26.7% over Nb_2O_5 and c-Nb_2O_5, respectively. On the other hand, NbO_x reached its highest formation rate of 55 μg h^{-1} $mg_{cat}{}^{-1}$ at the potential of −1.15 V, and it was larger than those over Nb_2O_5 and c-Nb_2O_5 (40.7 μg h^{-1} $mg_{cat}{}^{-1}$ and 13.8 μg h^{-1} $mg_{cat}{}^{-1}$, respectively).

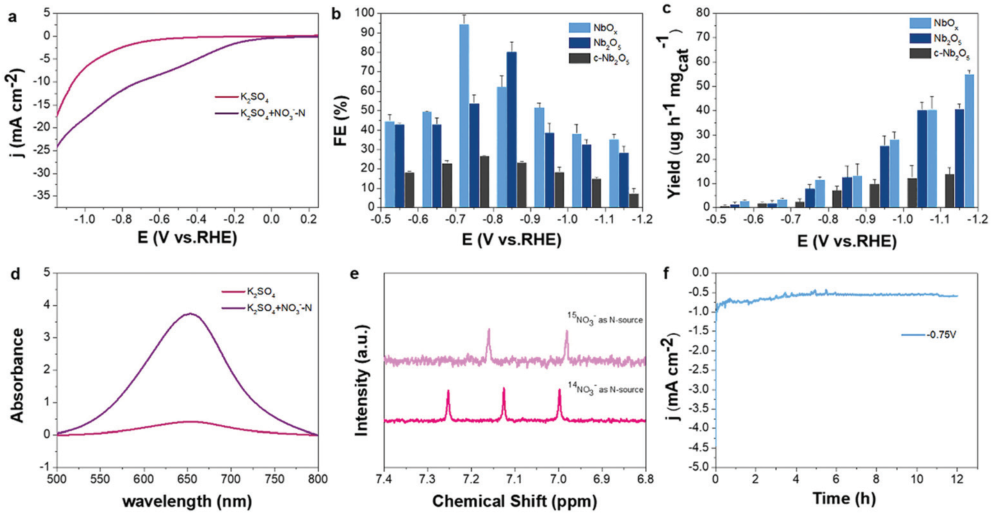

Fig. 3 (a) LSV curves in Ar-saturated 0. 5 M K_2SO_4 solution with and without NO_3^-. The scan rate was 10 mV s^{-1}. (b and c) FEs and the NH_3 formation rate (yield) of catalysts at different potentials. (d) UV-vis spectra of the electrolyte. (e) ^1H NMR spectra of the electrolyte after the NO_3^- reduction at −0.75 V using $^{14}NO_3^-$ and $^{15}NO_3^-$ as N sources. (f) Time-dependent current density curve over NbO_x at −0.75 V for 12 h.

Notably, NbO_x shows an evidently higher NH_3 formation rate and FE than those reported over non-noble-metal electrocatalysts for nitrate electroreduction to NH_3. Typical examples are TiO_{2-x} (FE 85.0%),[13] Co/CoO NSAs (FE 93.8%),[5] FC (FE 20%, NH_3 yield 23.8 mmol h^{-1} $g_{cat}{}^{-1}$),[33] Ir NTs (FE 84.7%),[34] and Fe-SnO_2 (FE 20.4%, yield 82.7 mg h^{-1} $mg_{cat}{}^{-1}$).[35] A more detailed comparison is shown in Table S1 (ESI†). The prominent activity of NbO_x can be attributed to the OVs, which improve nitrate electroreduction activity by modifying the surface binding energy of key intermediates. The presence of OVs leads to an acidic surface for strong adsorption towards $NO_3{}^-$, which further improved the reduction activity. Moreover, the oxygen atom in nitrate fills in OVs to weaken the N–O bonding and restrain the formation of byproducts, resulting in a high faradaic efficiency and ammonium yield. In addition, the spherical structure may facilitate the diffusion of reactants, the reaction intermediates and products during the process of electrolysis.[36,37]

Potentiostatic tests were measured at −0.75 V in the same electrolyte with the addition of different contents of $NO_3{}^-$ (100, 200, 500, 800, and 1000 ppm) for comparison. It can be seen from Fig. S6† that the faradaic efficiency and the NH_3 formation rate increased with the increasing nitrate concentration. They reached the highest value when the nitrate concentration was 1000 ppm. We also carried out electrolysis tests in an acidic electrolyte (0.1 M HCl + 1000 ppm $NO_3{}^-$). The highest faradaic efficiency for NH_3 formation was only 62.8%, which is much lower than that in the neutral electrolyte (0.5 M K_2SO_4). On the other hand, the overpotential of the reaction is relatively higher under alkaline electrolyte conditions. Therefore, the optimal electrolyte was a neutral electrolyte (0.5 M K_2SO_4) in this work.

To exclude the possible interference from the environment and system, controlled potential electrolysis over NbO_x in K_2SO_4 electrolyte without the addition of nitrate was also carried out. The corresponding UV-vis spectrum after electrolysis showed that NH_3 was not generated (Fig. 3d). It can be clearly observed that the difference with and without nitrate was quite obvious. All the discussions above indicate that the experimental values were authentic and reasonable. In order to further verify that the produced NH_3 was derived from the nitrate reduction, we also carried out the experiment using the same set-up over NbO_x with the addition of ^{15}N isotope-labeled nitrate. After the electrocatalytic reaction, the ^1H nuclear magnetic resonance (NMR) spectra of the electrolyte showed the representative double peaks of $^{15}NH_4{}^+$ at 6.98 and 7.10 ppm, while the ^1H NMR spectra of the electrolyte employing $K^{14}NO_3$ showed a typical triplet $^{14}NH_4{}^+$ signal (triple peaks of $^{14}NH_4{}^+$) (Fig. 3e). The results further confirmed that the formation of NH_3 originated from the electroreduction of nitrate.[38–40]

The stability of the NbO_x catalyst is another critical parameter in electrocatalysis. Fig. 3f shows the chronoamperometry curve over NbO_x for 12 h, in which the current density had no obvious decrease, confirming its excellent stability. In addition, after the NITRR, SEM showed that NbO_x still preserves its initial morphology (Fig. S7†). XPS analyses (Fig. S8 and 9†) revealed that the composition and chemical nature of the catalysts remained unchanged after a long-term electrolysis. All these observations indicate its excellent electrochemical stability under ambient conditions.[20]

In order to figure out the change in the valence states of surface species for NbO_x and Nb_2O_5 during the NITRR process, quasi-operando Nb 3d XPS spectra were obtained after holding −0.75 V *vs.* RHE for 30 min, and the results are given in Fig. 4. It was shown that the Nb 3d peaks of NbO_x had higher binding energy than those of Nb_2O_5, indicating the higher oxidized Nb species on the surface during the reaction. NbO_x has a stronger $NO_3{}^-$ adsorption due to the presence of OVs, and the oxygen atom in $NO_3{}^-$ fills in OVs during the reaction. However, the Nb^{5+} species in Nb_2O_5 would be reduced to a lower chemical state. Therefore, NbO_x has higher oxidized Nb species than Nb_2O_5 in the quasi-operando XPS spectra. They revealed that the electron density reconfiguration occurred on NbO_x, resulting in the enhancement of catalytic activity for the NITRR.[41–43]

In summary, NbO_x catalysts have been successfully designed and synthesized for efficient nitrate reduction to NH_3. The highest FE and formation rate of NH_3 could reach 94.5% and 55.0 μg h^{-1} $mg_{cat}{}^{-1}$, respectively. Such performance significantly exceeded most of the reports for electrochemical nitrate reduction to NH_3, which are higher than those reported over non-noble-metal electrocatalysts. Moreover, the catalyst also showed good durability. A detailed study indicated that the prominent activity of NbO_x can be attributed mainly to the nature of NbO_x and the OVs, which can improve the binding energy of key intermediates during the electrolysis. This work provides a promising method for the NITRR with high

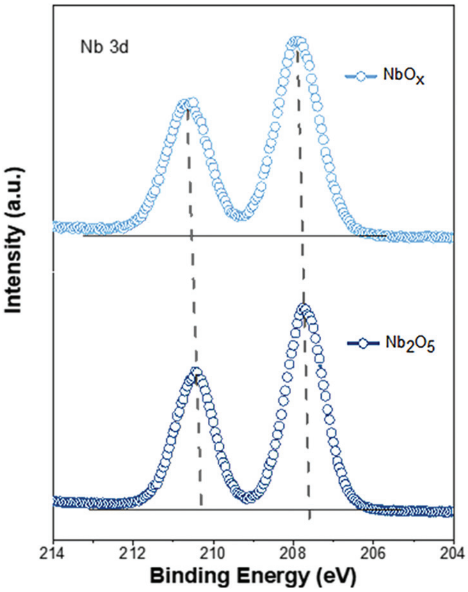

Fig. 4 Quasi-operando XPS spectra of the Nb 3d orbitals of the different catalysts.

efficiency. We believe that it may inspire new exploration and principles for designing electrocatalysts for NH_3 synthesis.

Author contributions

X. F. W., H. H. W., X. F. S. and B. X. H. proposed the project, designed the experiments, and wrote the manuscript; X. F. W. performed the whole experiments; W. W. G., X. D., M. E. C., S. T. H., J. X. Z., W. X., S. Q. J. and M. Y. H. performed the analysis of experimental data; H. H. W., X. F. S. and B. X. H. supervised the whole project.

Conflicts of interest

There are no conflicts to declare.

Acknowledgements

The work was supported financially by the National Key Research and Development Program of China (2017YFA0403101), the National Natural Science Foundation of China (22002172, 22121002), and the Chinese Academy of Sciences (QYZDY-SSW-SLH013).

Notes and references

1 B. H. R. Suryanto, H.-L. Du, D. Wang, J. Chen, A. N. Simonov and D. R. MacFarlane, *Nat. Catal.*, 2019, **2**, 290–296.

2 Y. Wang, W. Zhou, R. Jia, Y. Yu and B. Zhang, *Angew. Chem., Int. Ed.*, 2020, **59**, 5350–5354.

3 L. Hollevoet, F. Jardali, Y. Gorbanev, J. Creel, A. Bogaerts and J. A. Martens, *Angew. Chem., Int. Ed.*, 2020, **59**, 23825–23829.

4 L. Wu, W. Guo, X. Sun and B. Han, *Pure Appl. Chem.*, 2021, **93**, 777–797.

5 Y. Yu, C. Wang, Y. Yu, Y. Wang and B. Zhang, *Sci. China: Chem.*, 2020, **63**, 1469–1476.

6 M. Wang, S. Liu, H. Ji, T. Yang, T. Qian and C. Yan, *Nat. Commun.*, 2021, **12**, 3198.

7 S. Zhao, X. Lu, L. Wang, J. Gale and R. Amal, *Adv. Mater.*, 2019, **31**, e1805367.

8 X. Zhao, G. Hu, G. F. Chen, H. Zhang, S. Zhang and H. Wang, *Adv. Mater.*, 2021, e2007650.

9 X. Wang, S. Qiu, J. Feng, Y. Tong, F. Zhou, Q. Li, L. Song, S. Chen, K. H. Wu, P. Su, S. Ye, F. Hou, S. X. Dou, H. K. Liu, G. Q. Lu, C. Sun, J. Liu and J. Liang, *Adv. Mater.*, 2020, **32**, e2004382.

10 W. Guo, K. Zhang, Z. Liang, R. Zou and Q. Xu, *Chem. Soc. Rev.*, 2019, **48**, 5658–5716.

11 C. Yang, Y. Zhu, J. Liu, Y. Qin, H. Wang, H. Liu, Y. Chen, Z. Zhang and W. Hu, *Nano Energy*, 2020, **77**, 105126.

12 J. Deng, J. A. Iñiguez and C. Liu, *Joule*, 2018, **2**, 846–856.

13 R. Jia, Y. Wang, C. Wang, Y. Ling, Y. Yu and B. Zhang, *ACS Catal.*, 2020, **10**, 3533–3540.

14 Y. Wang, C. Liu, B. Zhang and Y. Yu, *Sci. China Mater.*, 2020, **63**, 2530–2538.

15 Y. Wang, A. Xu, Z. Wang, L. Huang, J. Li, F. Li, J. Wicks, M. Luo, D. H. Nam, C. S. Tan, Y. Ding, J. Wu, Y. Lum, C. T. Dinh, D. Sinton, G. Zheng and E. H. Sargent, *J. Am. Chem. Soc.*, 2020, **142**, 5702–5708.

16 Z. Y. Wu, M. Karamad, X. Yong, Q. Huang, D. A. Cullen, P. Zhu, C. Xia, Q. Xiao, M. Shakouri, F. Y. Chen, J. Y. T. Kim, Y. Xia, K. Heck, Y. Hu, M. S. Wong, Q. Li, I. Gates, S. Siahrostami and H. Wang, *Nat. Commun.*, 2021, **12**, 2870.

17 J. Y. Zhu, Q. Xue, Y. Y. Xue, Y. Ding, F. M. Li, P. Jin, P. Chen and Y. Chen, *ACS Appl. Mater. Interfaces*, 2020, **12**, 14064–14070.

18 G.-F. Chen, Y. Yuan, H. Jiang, S.-Y. Ren, L.-X. Ding, L. Ma, T. Wu, J. Lu and H. Wang, *Nat. Energy*, 2020, **5**, 605–613.

19 J. Lim, C.-Y. Liu, J. Park, Y.-H. Liu, T. P. Senftle, S. W. Lee and M. C. Hatzell, *ACS Catal.*, 2021, **11**, 7568–7577.

20 W. Kong, Z. Liu, J. Han, L. Xia, Y. Wang, Q. Liu, X. Shi, Y. Wu, Y. Xu and X. Sun, *Inorg. Chem. Front.*, 2019, **6**, 423–427.

21 L. Huang, J. Wu, P. Han, A. M. Al-Enizi, T. M. Almutairi, L. Zhang and G. Zheng, *Small Methods*, 2018, **3**, 1800386.

22 C. Zhang, S. Liu, T. Chen, Z. Li and J. Hao, *Chem. Commun.*, 2019, **55**, 7370–7373.

23 X. W. Lv, Y. Liu, R. Hao, W. Tian and Z. Y. Yuan, *ACS Appl. Mater. Interfaces*, 2020, **12**, 17502–17508.

24 R. Zhang, H. Guo, L. Yang, Y. Wang, Z. Niu, H. Huang, H. Chen, L. Xia, T. Li, X. Shi, X. Sun, B. Li and Q. Liu, *ChemElectroChem*, 2019, **6**, 1014–1018.

25 A. Naldoni, M. Allieta, S. Santangelo, M. Marelli, F. Fabbri, S. Cappelli, C. L. Bianchi, R. Psaro and V. Dal Santo, *J. Am. Chem. Soc.*, 2012, **134**, 7600–7603.

26 X. Wang, X. Li, J. Mu, S. Fan, X. Chen, L. Wang, Z. Yin, M. Tade and S. Liu, *ACS Appl. Mater. Interfaces*, 2019, **11**, 41988–41999.

27 Y. J. Hao, B. Liu, L. G. Tian, F. T. Li, J. Ren, S. J. Liu, Y. Liu, J. Zhao and X. J. Wang, *ACS Appl. Mater. Interfaces*, 2017, **9**, 12687–12693.

28 A. Sinhamahapatra, J.-P. Jeon and J.-S. Yu, *Energy Environ. Sci.*, 2015, **8**, 3539–3544.

29 Z. Geng, X. Kong, W. Chen, H. Su, Y. Liu, F. Cai, G. Wang and J. Zeng, *Angew. Chem., Int. Ed.*, 2018, **57**, 6054–6059.

30 X. Xing, H. Zhu, M. Zhang, L. Hou, Q. Li and J. Yang, *Catal. Sci. Technol.*, 2018, **8**, 3629–3637.

31 Y.-H. Chin, J.-C. Sin, S.-M. Lam and A. R. Mohamed, *J. Mater. Sci.: Mater. Electron*, 2018, **30**, 1739–1750.

32 X. Yu, B. Kim and Y. K. Kim, *ACS Catal.*, 2013, **3**, 2479–2486.

33 Y. Li, S. Xiao, X. Li, C. Chang, M. Xie, J. Xu and Z. Yang, *Mater. Today Phys.*, 2021, **19**, 100431.

34 J. Y. Zhu, Q. Xue, Y. Y. Xue, Y. Ding, F. M. Li, P. Jin, P. Chen and Y. Chen, *ACS Appl. Mater. Interfaces*, 2020, **12**, 14064–14070.

35 L. Zhang, M. Cong, X. Ding, Y. Jin, F. Xu, Y. Wang, L. Chen and L. Zhang, *Angew. Chem., Int. Ed.*, 2020, **59**, 10888–10893.

36 M. Nazemi, S. R. Panikkanvalappil and M. A. El-Sayed, *Nano Energy*, 2018, **49**, 316–323.

37 Y. Zhang, W. Qiu, Y. Ma, Y. Luo, Z. Tian, G. Cui, F. Xie, L. Chen, T. Li and X. Sun, *ACS Catal.*, 2018, **8**, 8540–8544.

38 C. Hu, X. Chen, J. Jin, Y. Han, S. Chen, H. Ju, J. Cai, Y. Qiu, C. Gao, C. Wang, Z. Qi, R. Long, L. Song, Z. Liu and Y. Xiong, *J. Am. Chem. Soc.*, 2019, **141**, 7807–7814.

39 X. Yang, J. Nash, J. Anibal, M. Dunwell, S. Kattel, E. Stavitski, K. Attenkofer, J. G. Chen, Y. Yan and B. Xu, *J. Am. Chem. Soc.*, 2018, **140**, 13387–13391.

40 X. Yang, S. Kattel, J. Nash, X. Chang, J. H. Lee, Y. Yan, J. G. Chen and B. Xu, *Angew. Chem., Int. Ed.*, 2019, **58**, 13768–13772.

41 W. Guo, X. Tan, J. Bi, L. Xu, D. Yang, C. Chen, Q. Zhu, J. Ma, A. Tayal, J. Ma, Y. Huang, X. Sun, S. Liu and B. Han, *J. Am. Chem. Soc.*, 2021, **143**, 6877–6885.

42 Z. Xiao, Y. C. Huang, C. L. Dong, C. Xie, Z. Liu, S. Du, W. Chen, D. Yan, L. Tao, Z. Shu, G. Zhang, H. Duan, Y. Wang, Y. Zou, R. Chen and S. Wang, *J. Am. Chem. Soc.*, 2020, **142**, 12087–12095.

43 J. Geng, S. Ji, H. Xu, C. Zhao, S. Zhang and H. Zhang, *Inorg. Chem. Front.*, 2021, **8**, 5209–5213.